Check for updates

A commercially scalable MOF adsorbent Cu-BTC for helium recovery from natural gas: performance and mechanism studies at room temperature and lower temperatures†

Shoucheng Cui, [ID] [abc] Baosheng Chen, [abc] Jiasi Zhao, [abc] Hongbo Xu,*[ab] Nan Peng[ab] and Liqiang Liu*[abc]

The performance and mechanism of the adsorptive separation of some helium-based gas mixtures in a metal–organic framework (MOF) Cu-BTC at room and lower temperature were studied for helium recovery from natural gas. Both GCMC simulations and experimental tests were used to obtain adsorption isotherms for Cu-BTC with CO_2, CH_4, N_2, and He adsorbates. The ideal adsorbed solution theory (IAST) and GCMC simulations were applied to calculate the CO_2/He, CH_4/He, and N_2/He selective adsorption coefficients respectively. Additionally, adsorption breakthrough experiments were conducted to test the adsorption breakthrough curves of CO_2/He, CH_4/He, N_2/He, and CH_4/N_2/He gas mixtures on Cu-BTC. The study found that Cu-BTC exhibited a favorable separation effect for CO_2/He, CH_4/He, and N_2/He gas mixtures, with the separation efficiency at room temperature following the order of CO_2/He > CH_4/He > N_2/He. Further investigations revealed that lowering the temperature significantly improved the adsorptive selectivity of Cu-BTC for CH_4/He and N_2/He mixtures, as well as the separation efficiency for the CH_4/N_2/He ternary gas mixture. Based on simulation data, the study also calculated the isosteric heat of adsorption, adsorption energy distribution, adsorbate density distribution, and binding energy to analyze the mechanism of competitive adsorption of the studied helium-based gas mixtures on Cu-BTC.

Introduction

Natural gas is widely regarded as the optimal energy resource for the transition between high-carbon fossil fuels and renewable energy. At present, it is the only hydrocarbon energy source that will significantly lower greenhouse gas emissions and other pollutants.[1] It is a mixture containing various hydrocarbons, CO_2, N_2, H_2, He, and other components, among which helium is a valuable and scarce resource. Helium's unique physical properties, such as an extremely low boiling point, small molecular size, high specific heat, and high thermal conductivity,

make it irreplaceable in modern industrial production, scientific research, and medical technology.[2,3] The helium content in natural gas is usually very low, with most sources containing less than 1% helium.[3] The helium content of natural gas may vary dramatically from region to region, with high levels reaching up to 10%, while low levels may be below 0.003%.[4] Efficiently recovering helium from natural gas is of great significance both for the utilization of helium resources and for enhancing the heating value of natural gas. The main methods for recovering helium from natural gas include cryogenic distillation, membrane-based separations, and adsorption-based separations,[5,6] which can be used in combination to exploit their respective advantages, with adsorption-based separations often being a crucial procedure in accomplishing high-purity helium. For the adsorption-based separation process, the adsorbent is foundational and essential. The selected adsorbent is supposed to have high adsorption capacity and high selectivity.

Metal–organic framework (MOF) materials consist of inorganic metal centers and organic ligands. Due to their large specific surface area, substantial pore volume, tunable pore size, and ease of functionalization, MOFs have recently

[a] *Technical Institute of Physics and Chemistry, Chinese Academy of Sciences, Beijing 100190, China. E-mail: hbxu@mail.ipc.ac.cn, lqliu@mail.ipc.ac.cn*
[b] *Key Laboratory of Cryogenic Science and Technology, Beijing 100190, China*
[c] *University of Chinese Academy of Sciences, Beijing 100049, China*

attracted significant attention from researchers in the field of gas adsorption and separation.[7,8] They show promising applications in H_2 storage,[9] CO_2 capture,[10] removal of harmful gases,[11] separation of hydrocarbon gas mixtures,[12,13] and gas isotope separation.[14] MOF materials can be applied to helium extraction from natural gas through adsorption-based or membrane-based separation methods: Kadioglu et al.[15] used GCMC and EMD simulations to predict the separation performance of 139 different MOF membranes for CH_4/He gas mixtures and found that a multitude of MOF membranes exceeded the Robeson upper bound. Wang et al.,[16] using first-principle calculations and molecular dynamics simulations, studied the permeability and filtration performance of He in 2D Fe-PTC and Ni-PTC membranes in various helium-containing gas mixtures, discovering that both Fe-PTC and Ni-PTC exhibited excellent He separation performance. Grenev et al.[17] screened 5156 MOFs for helium extraction from natural gas, studying both membrane-based and adsorption-based separation methods. Their research indicated that for CH_4/N_2/He mixtures, most MOFs have a higher selectivity for CH_4 than for N_2. They also identified the ideal structural parameters for MOF adsorbents selective adsorption: porosity (< 0.17), pore volume (0.01–0.12 cm^3 g^{-1}), and specific surface area (100–1000 m^2 g^{-1}). Overall, most research on MOFs for helium extraction from natural gas has focused on membrane-based methods, with fewer studies exploring adsorption-based methods. Meanwhile, research on the application of MOFs in natural gas adsorption-based helium extraction has primarily focused on molecular simulation and material screening, with relatively few experimental studies. Furthermore, most traditional adsorbents, such as activated carbon and zeolite molecular sieves, require significantly low temperatures (far below ambient temperature) to achieve optimal adsorptive separation performance. However, studies on the adsorptive separation of gas mixtures using MOFs at low temperatures remain limited. In engineering applications, some studies on the natural gas adsorption-based helium extraction process have been conducted using traditional adsorbents like activated carbon and zeolites, mainly focusing on the optimization of pressure swing adsorption (PSA) processes.[18–20] Given the superior adsorption capacity and selectivity of MOFs compared to conventional adsorbents, their application in helium recovery processes holds great promise for achieving improved purification performance. In summary, investigating the adsorptive separation performance and mechanisms of MOFs for helium-containing gas mixtures at different temperatures can not only deepen the understanding of competitive adsorption mechanisms in MOFs at low temperatures but also provide valuable insights for their application in natural gas adsorption-based helium extraction.

Cu-BTC, also known as HKUST-1, was first synthesized by the Hong Kong University of Science and Technology. It features Cu as the metal center and benzene-1,3,5-tricarboxylate as the organic ligand, with a high density of Cu^{2+} open sites. Its preparation method is relatively mature, and the cost is lower compared to other MOF materials, making it promising for applications. Recently, it has captured substantial interest in the field of gas adsorption and separation.[21–24] Currently, there exists research mainly centralizing on utilizing Cu-BTC in membrane technology for helium separation: Ali Akbari et al.[25] synthesized hybrid matrix membranes by employing Cu-BTC particles created through a three-layer synthesis technique. They tested the separation performance of these membranes for CH_4/He and N_2/He gas mixtures. The study found that reducing the particle size of Cu-BTC gave rise to a more uniform distribution of MOF fillers, resulting in enhanced separation performance. Additionally, membranes containing 40% wt MOF particles showed demonstrated the highest selectivity, with He/CH_4 selectivity reaching 369.1 and He/N_2 selectivity at 265.8.

In this study, we utilized Cu-BTC for adsorption processes to purify helium by removing CO_2, CH_4, and N_2 impurities in natural gas. We employed a combination of grand canonical Monte Carlo (GCMC) simulations and experimental techniques to determine the adsorption isotherms for CO_2, CH_4, N_2, and He on Cu-BTC individually. To calculate the selective adsorption coefficients for CO_2/He, CH_4/He, and N_2/He, both GCMC simulations and ideal adsorbed solution theory (IAST) were used. Breakthrough adsorption experiments were carried out to evaluate the actual separation efficiency of Cu-BTC for gas mixtures including CO_2/He, CH_4/He, N_2/He, and CH_4/N_2/He. Moreover, we explored the impact of temperature decline on the performance of Cu-BTC in extracting helium from CH_4 and N_2 impurities. To further understand the competitive adsorption mechanism on Cu-BTC, we employed GCMC simulations to calculate the isosteric heat of adsorption, adsorption energy distribution, and adsorbate density distribution. By using density functional theory (DFT) calculations, we eventually determined the binding energy data for each adsorption site in Cu-BTC with the adsorbates CO_2, CH_4, N_2, and He. In summary, this study employed a combined approach of molecular simulation and experimental testing to investigate the performance and mechanism of selective adsorption from multiple perspectives. Currently, the application of MOF materials in industrial production remains limited. By providing data on the actual performance of Cu-BTC in separating helium-containing gas mixtures at different temperatures, this research offers valuable insights for the use of commercially promising MOF material Cu-BTC in the adsorption stage of helium recovery from natural gas. Moreover, the investigation of competitive adsorption mechanisms contributes to the guidance of MOF modification and design, thereby promoting, to some extent, the application of MOFs in the field of helium recovery from natural gas.

Experimental

Materials and methods

Material. The material used in this work is copper 1,3,5-benzenetricarboxylate, Cu-BTC, purchased from Merck

Chemical Technology Co., Ltd. It is in the form of a blue powder with a particle size distribution of 15.96 μm (D50), prepared *via* a solvothermal method. Its crystal structure (primitive cell) is shown in Fig. 1. For material characterization, the study tested the scanning electron microscopy (SEM) images of the Cu-BTC powder, as shown in Fig. S1,† using a Hitachi Regulus 8220 instrument. The specific surface area, total pore volume, and pore size distribution of the powder material were also tested using the BET method with a BSD-660S A6B3T physical adsorption analyzer. This involved measuring the adsorption–desorption isotherms of N_2 on Cu-BTC at 77.3 K, and calculating the BET specific surface area using the BET multi-point method. The results of the adsorption–desorption isotherms are shown in Fig. S2,† and the specific surface area calculation method is detailed in the ESI.† Table 1 presents the BET specific surface area, total pore volume, and average pore diameter of the material. The pore size distribution based on pore volume and pore area is shown in Fig. S3(a) and (b),† respectively. It can be seen that the Cu-BTC sample contains only micropores (pore size 0.35–2 nm) and mesopores (pore size 2–50 nm), with a high proportion of micropores, indicating a well-developed porous structure.

Molecular simulation. GCMC simulations were used to calculate the adsorption isotherms, isosteric heat of adsorption, adsorption energy distribution, and adsorbate density distribution of single-component gases CO_2, CH_4, N_2, and He on Cu-BTC. The simulations were conducted using the Sorption module in the Materials Studio software, with the Cu-BTC crystal structure downloaded from the Cambridge Crystallographic Data Centre (CCDC) and the primitive cell used for calculations. The COMPASS II force field was employed in the simulations, considering only physical adsorption, where the interactions between adsorbate molecules and adsorbent were the sum of van der Waals forces and electrostatic forces, with van der Waals forces calculated using the LJ potential. For the adsorbate molecules CO_2, CH_4, and N_2, atomic charge data are shown in Table S1,† and geometric optimization was performed using the Forcite module, with optimized bond length data shown in Table S1.† For the adsorbent Cu-BTC crystal, atomic charges were taken from the DDEC atomic charges calculated by Nazarian *et al.*[26] For the calculation of adsorption isotherms, the task type was set to adsorption isotherm, the

algorithm was selected as metropolis, and the accuracy was set to fine. The equilibration steps were 10^5, and the pressure range for the calculation was 0–3000 kPa. The atomic charges were set to use current, the electrostatic summation method was Ewald & Group, and the van der Waals summation method was atom based with a cutoff radius of 15.5 Å. For the CO_2 adsorbate, due to its high boiling point (195 K, 101.325 kPa), only the adsorption isotherm at ambient temperature (298 K) was calculated. For CH_4, N_2, and He adsorbates, calculations were performed at both 298 K and 200 K. The isosteric heat of adsorption data was obtained simultaneously with the calculation of adsorption isotherms, using the formula shown in eqn (1):

$$Q_{st} = RT - \frac{\langle UN \rangle - \langle U \rangle \langle N \rangle}{\langle N^2 \rangle - \langle N \rangle^2} \quad (1)$$

where Q_{st} is the isosteric heat of adsorption, R is the universal gas constant, T is the temperature, U is the energy value, N is the number of molecules, $\langle \ \rangle$ represents the ensemble average. For the calculation of adsorption energy distribution and adsorbate density distribution, the task type was selected as fixed pressure, the method as metropolis, and the accuracy as fine. The equilibration steps were set to 10^5. Use current was chosen for atomic charges, Ewald & Group for the summation method of electrostatic forces, and Atom based for the summation method of van der Waals forces, with a cutoff radius of 15.5 Å. The calculation pressure was 101 kPa. For CO_2, the calculation temperature was 298 K, and for CH_4, N_2, and He, the calculation temperatures were 298 K and 200 K.

DFT was used to calculate the adsorption binding energies of CO_2, CH_4, N_2, and He molecules at different adsorption sites on Cu-BTC. The calculation was based on the adsorbate density distribution obtained from GCMC simulations, using the DMol3 module in Materials Studio. After inserting the adsorbate molecules into the adsorbent model, Geometry Optimization tasks were applied for geometric optimization. Subsequently, energy tasks were used to calculate the structural energy of the adsorbent ($E_{adsorbent}$), the energy of the adsorbate molecule ($E_{adsorbate}$), and the total system energy (E_{total}). The adsorption binding energy ($E_{binding}$) was computed using eqn (2).

$$E_{binding} = E_{total} - (E_{adsorbent} + E_{adsorbate}) \quad (2)$$

The calculation accuracy was set to fine, the functionals chosen are GGA and PBE, core treatment was set to DFT semi-core Pseudopots, SCF tolerance is 10^{-6}, and the global orbital cutoff value was 5.2 Å.

Experiments. The adsorption isotherm data were measured using the BSD-PH fully automatic high-pressure gas adsorption analyzer based on the volumetric method. To facilitate comparison with molecular simulation results, the pressure range of the measurements remained 0–3000 kPa. For the choice of test temperatures, CO_2 was tested at 298 K, while CH_4, N_2, and He were tested at 200 K. Low-temperature
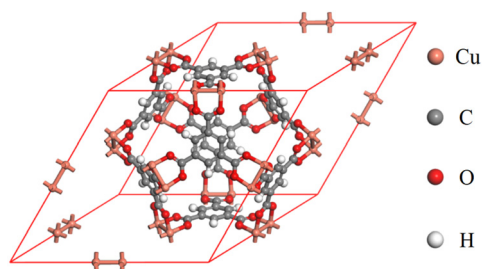

Fig. 1 Cu-BTC crystal structure.

- Cu
- C
- O
- H

Table 1 BET specific surface area, total pore volume, and average pore diameter of Cu-BTC

BET specific surface area A^a (m^2 g^{-1})	Total pore volume V^b (cm^3 g^{-1})	Average pore diameter d^c (nm)
1780.68	0.7278	1.635

^{a} Tested by the BET multi-point method. ^{b} Tested at $P/P_0 = 0.99$. ^{c} $d = 4 V/A$.

control was achieved using the BSD-LNT low-temperature constant temperature system, which utilizes liquid nitrogen and its vapor to achieve precise temperature control with an accuracy better than 0.1 K. Additionally, to align with simulations, the experimentally measured excess adsorption amount (n_e) needs to be converted to absolute adsorption amount (n_a), as shown by eqn (3).

$$n_a = n_e + \rho_g V_a \tag{3}$$

where ρ_g is the bulk phase density and V_a is the total pore volume of the adsorbent.

The adsorption breakthrough curve tests were conducted using the BSD-MAB multi-component adsorption breakthrough curve analyzer. Gas concentration detection relied on the BSD-MASS online mass spectrometry gas analysis system, with a resolution of less than 0.5 ppm. The testing pressure was atmospheric pressure (101.325 kPa). For the CO_2/He (50:50) mixed gas, the testing temperature is 298 K. For the CH_4/He (50:50), N_2/He (50:50), and $CH_4/N_2/He$ (33:33:33) mixed gases, testing was performed at 298 K, 200 K, and 150 K respectively. During testing, the flow rate for each component in each mixed gas was set to 5 sccm.

Calculation of the selective adsorption coefficients. The selective adsorption coefficient of the adsorbent for binary mixed gases is defined by eqn (4).

$$S_{i/j} = \frac{x_i/x_j}{y_i/y_j} \tag{4}$$

where i and j represent two different gas components in a binary mixed gas, $S_{i/j}$ denotes the selective adsorption coefficient, and x and y respectively denote the mole fractions of the gas components in the adsorbed phase and gas phase. The calculation of selective adsorption coefficients was performed using IAST and GCMC simulations. For the IAST method, it predicts the adsorption selectivity of the adsorbent for multi-component mixed gases based on single-component adsorption isotherm data. In this study, for CO_2/He (50:50), CH_4/He (50:50), and N_2/He (50:50) mixed gases, the selective adsorption coefficients were calculated using experimental adsorption isotherm data. The conditions for calculation were temperatures of 298 K and 200 K, and pressures ranging from 0 to 3000 kPa. Specific calculation methods are detailed in the supplementary materials. For fitting the adsorption isotherms, the adsorption isotherms

for He at 298 K and 200 K were fitted using the Henry model, as shown in eqn (5), while the remaining gases were fitted using the Langmuir model, as shown in eqn (6).

$$n = k_H p \tag{5}$$

$$n = n_m \frac{bp}{1 + bp} \tag{6}$$

where n represents adsorption capacity, p denotes pressure, k_H is the Henry constant, n_m is monolayer saturation adsorption capacity, and b is the Langmuir constant. For GCMC simulation, in order to compare with the selectivity obtained from IAST, the temperature and pressure conditions used for calculations were identical to those of IAST. The calculations were conducted using the Sorption module in Materials Studio, employing the Adsorption Isotherm task. CO_2/He (50:50), CH_4/He (50:50), and N_2/He (50:50) binary gas mixtures were computed by adjusting the partial pressures of each component to achieve the desired feed ratios, with other settings similar to those used for single-component adsorption isotherms. After obtaining the adsorption isotherm data for the mixed gas, eqn (4) was used to calculate the selective adsorption coefficients.

Results and discussion

Single-component adsorption isotherms

The GCMC simulation and experimental data for the single-component gas adsorption isotherms of CO_2, CH_4, N_2, and He on Cu-BTC, along with their respective fitting curves, are shown in Fig. 2(a)–(d). The adsorption isotherms of He at 298 K and 200 K were fitted using the Henry model, while the rest were fitted using the Langmuir model. The fitting parameters for the adsorption isotherms are listed in Table S2.†
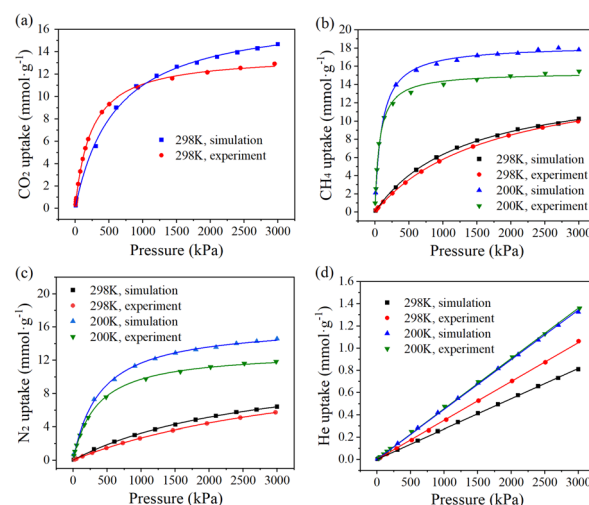

Fig. 2 Adsorption isotherm simulation and experimental results for CO_2 at 298 K (a), CH_4 at 298 K and 200 K (b), N_2 at 298 K and 200 K (c), and He at 298 K and 200 K (d) in Cu-BTC; pressure ranges from 0 to 3000 kPa.

According to Table S2,† all R^2 values are greater than 0.995, indicating that the data fitting is quite accurate. As seen in Fig. 2, the GCMC simulation results are generally consistent with the experimental results. According to the IUPAC classification, the adsorption isotherms of CO_2, CH_4, N_2, and He on Cu-BTC are all Type I adsorption isotherms. At 298 K, the adsorption capacity of Cu-BTC for the four adsorbates follows the order: $CO_2 > CH_4 > N_2 >$ He. For CH_4, N_2, and He adsorbates, as the temperature decreases to 200 K, the adsorption capacity increases, and the order remains $CH_4 > N_2 >$ He. The adsorption of He on Cu-BTC is relatively weak at both 298 K and 200 K, with the adsorption isotherms approaching a straight line, approximating Henry's law. At the same temperature, Cu-BTC's strongest adsorption is for CO_2 due to the high polarizability of CO_2 molecules (2.93 Å^3)[27] and the presence of a quadrupole moment, which enhances the electrostatic interactions with the adsorbent surface and open metal sites. Additionally, the small kinetic diameter of CO_2 molecules (3.3 Å)[28] facilitates their diffusion into the adsorbent's pore structure. Both CH_4 and N_2 molecules are nonpolar with lower polarizability, CH_4 at 2.6 Å^3 and N_2 at 1.76 Å^3, and have larger kinetic diameters, CH_4 at 3.8 Å and N_2 at 3.6 Å[28], resulting in weaker adsorption on Cu-BTC compared to CO_2. Among the four adsorbates, He has the smallest polarizability (0.205 Å^3)[29] and kinetic diameter (2.55 Å),[30] leading to the weakest adsorption on Cu-BTC. The experimental results from this study indicate that Cu-BTC exhibits a higher adsorption capacity for CH_4 and N_2 compared to some traditional adsorbents such as activated carbon and zeolites.[31–33] Cu-BTC's stronger affinity for CH_4 and N_2 is beneficial for helium purification. Meanwhile, at 298 K and 1 bar, the CO_2 adsorption capacity of Cu-BTC is higher than that of Mg-MOF-74,[34] MOF-205,[35] and MOF-177.[36] The adsorption capacities for CH_4, N_2, and He are all higher than those of MIL-101 and MIL-53.[37] At 298 K and 5 bar, the CH_4 adsorption capacity is higher than that of MIL-100-Cr and MIL-100-Fe,[38] which may be attributed to the high density of open metal sites in Cu-BTC.

CO_2/He, CH_4/He and N_2/He selectivity

The relationship curves between IAST selectivity and pressure for the Cu-BTC adsorption of CO_2/He (50 : 50), CH_4/He (50 : 50), and N_2/He (50 : 50) gas mixtures are shown in Fig. 3(a)–(c). As seen in Fig. 3, the IAST selectivity of Cu-BTC for CO_2/He, CH_4/He, and N_2/He decreases with increasing pressure. This is because, at low pressure, the number of adsorption sites on the adsorbent is sufficient, and the adsorption capacity of each component in the gas mixture is close to their single-component adsorption capacity. As the pressure increases, the adsorption capacity of the gas mixture on the adsorbent increases, leading to competition for adsorption sites among the components, thereby reducing selectivity. At room temperature (298 K), Cu-BTC already shows good selectivity for CO_2/He, with the selectivity order being CO_2/He > CH_4/He > N_2/He. As the temperature decreases to 200 K, the selectivity for CH_4/He and
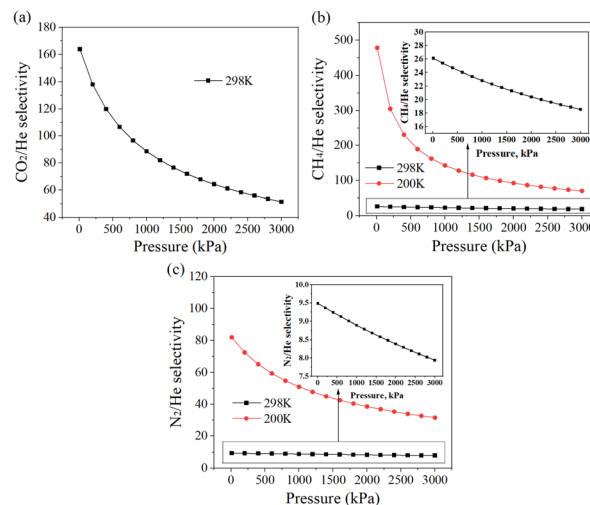

Fig. 3 The relationship between IAST selectivity coefficients and pressure for Cu-BTC at 298 K for CO_2/He (50 : 50) (a), at 298 K and 200 K for CH_4/He (50 : 50) (b), and at 298 K and 200 K for N_2/He (50 : 50) (c) gas mixtures; pressure ranges from 0 to 3000 kPa.

N_2/He significantly increases, with the selectivity order remaining CH_4/He > N_2/He. To discuss the accuracy of IAST predictions for selectivity in this study, GCMC simulations were also used to calculate the selectivity adsorption coefficients of Cu-BTC for CO_2/He (50 : 50), CH_4/He (50 : 50), and N_2/He (50 : 50) gas mixtures under the same temperature and pressure conditions. The results are shown in Fig. S4(a)–(c).† It can be seen that the selectivity of Cu-BTC for each gas mixture does not strictly monotonically decrease with increasing pressure at all temperatures, especially for the CO_2/He gas mixture, where the trend of selectivity change with pressure significantly differs from the IAST predictions, rendering the previous explanation for IAST predictions seemingly unjustifiable. Additionally, there are noticeable numerical differences between the selectivity calculated by GCMC and the values predicted by IAST. These phenomena indicate that IAST, which calculates adsorption selectivity based on single-component adsorption isotherms, is less reliable compared to GCMC calculations that consider multicomponent competitive adsorption. IAST predictions of adsorption selectivity may produce errors due to the non-ideality of the gas phase and interactions between adsorbate molecules, and IAST lacks consideration of competitive adsorption. Predictions for adsorbents with heterogeneous surface energy may also deviate from actual situations.[39] However, for both IAST predictions and GCMC simulation results, the order of adsorption selectivity at 298 K is consistent as CO_2/He > CH_4/He > N_2/He, and the rule that lowering the temperature increases the selectivity for CH_4/He and N_2/He is also consistent.

Isosteric heat of adsorption

The GCMC calculation results of the isosteric heats of adsorption for CO_2, CH_4, N_2, and He on Cu-BTC are shown in Fig. 4(a)–(d). The isosteric heat of adsorption (Q_{st}) refers to the
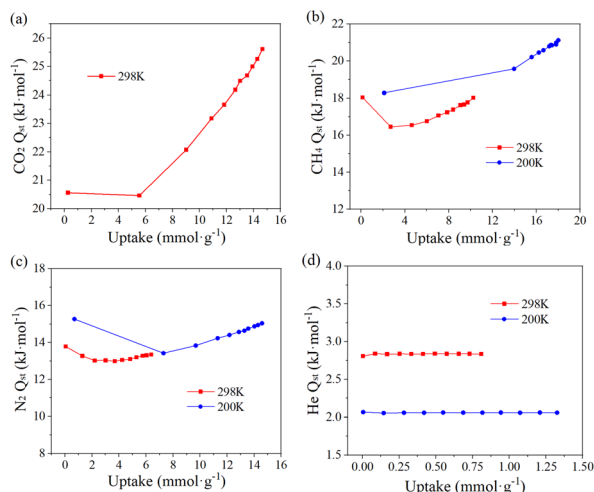
Fig. 4 Results of the heat of adsorption for CO_2 at 298 K (a), CH_4 at 298 K and 200 K (b), N_2 at 298 K and 200 K (c), and He at 298 K and 200 K (d) in Cu-BTC.

amount of energy released by the system when an infinitesimally small amount of gas molecules is adsorbed at a constant adsorption capacity. It represents the instantaneous enthalpy change during the adsorption process. They can be used to characterize the affinity between the adsorbate molecules and the adsorbent framework: the stronger the affinity, the greater the isosteric heat of adsorption. From Fig. 4, it can be seen that at 298 K, the order of Q_{st} for the four adsorbates in Cu-BTC is $CO_2 > CH_4 > N_2 > He$. For CH_4 and N_2 as the temperature decreases to 200 K, their Q_{st} values increase, maintaining the order $CH_4 > N_2$. These patterns are consistent with the adsorption capacity order of the four adsorbates in Cu-BTC, further confirming that the adsorption strength of Cu-BTC for the four adsorbates at the same temperature follows the order $CO_2 > CH_4 > N_2 > He$. For CO_2, CH_4, and N_2, the Q_{st} values change with increasing adsorption amounts, indicating that the energy distribution of adsorption on the Cu-BTC surface is uneven for these three adsorbates. According to the Q_{st} data for CO_2 and CH_4 at 298 K and for N_2 at 298 K and 200 K, Q_{st} initially decreases and then increases with increasing adsorption amounts. The high Q_{st} at low adsorption amounts suggests that the Cu-BTC surface has strong electrostatic and dispersion forces for CO_2, CH_4, and N_2 gas molecules, which corresponds to the large number of unsaturated metal sites within the Cu-BTC framework. As the adsorption amount increases, the interactions between gas molecules strengthen, leading to an increase in Q_{st} for CO_2, CH_4, and N_2 in Cu-BTC at higher adsorption amounts. For He, the Q_{st} changes very little with increasing adsorption amounts, indicating that the energy distribution of adsorption on the Cu-BTC surface is relatively uniform for He. The relationship between the isosteric heat of adsorption (Q_{st}) and temperature is influenced by factors such as surface heterogeneity, lateral interactions, and surface coverage.[40,41] Based on the above analysis, for He adsorbate, the adsorption energy on the Cu-BTC surface is more uniform compared to CO_2, CH_4, and N_2

adsorbates. Additionally, since the critical temperature of He is significantly lower than that of CO_2, CH_4, and N_2, the lateral interactions between He adsorbate molecules at 200 K and 298 K are much weaker than those of the other three adsorbates. As a result, the relationship between Q_{st} and temperature for He adsorbate exhibits a different trend from that of the other three adsorbates, increasing with rising temperature.

Adsorbate density and adsorption energy distribution

The density distributions of CO_2, CH_4, N_2, and He in Cu-BTC at 298 K and 101 kPa are shown in Fig. 5(a)–(d). If the regions with higher adsorbate molecule density are defined as adsorption sites, it can be seen from Fig. 5(a)–(d) that there are two types of adsorption sites in Cu-BTC, as illustrated in Fig. 5(e). For CO_2, CH_4, and N_2, the adsorption is stronger than for He. The adsorbate density distribution shows that these three adsorbates are relatively concentrated, with site A having weaker adsorption than site B. For He, the distribution is more dispersed, indicating weaker adsorption, with little difference in the strength of adsorption between sites A and B. Meanwhile, as shown in Fig. 5, the adsorbates CO_2, CH_4, and N_2 exhibit the highest probability of being distributed near the open metal sites, indicating that the open Cu metal sites in Cu-BTC possess a high adsorption affinity for these gases. To some extent, this reflects that the open metal sites play a dominant role in governing the adsorption selectivity of Cu-BTC toward helium-containing gas mixtures. This study also calculated the adsorption energy distributions of CO_2, CH_4, N_2, and He in Cu-BTC at 101 kPa, 298 K, and 200 K to further analyze the adsorption mechanisms of these four adsorbates in Cu-BTC. The results are shown in Fig. 6(a)–(c). From Fig. 6, it can be seen that the energy range corresponding to the peak in the adsorption energy distribution for CO_2, CH_4, and N_2 is significantly larger than that for He, further indicating the preferential adsorption of these three adsorbates by Cu-BTC.
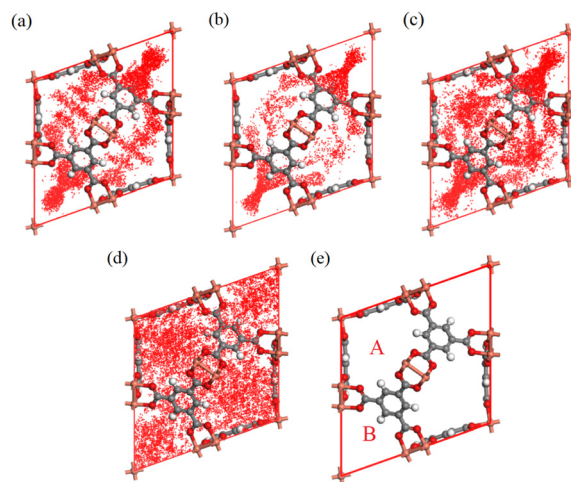

Fig. 5 Results of the density distributions of CO_2 (a), CH_4 (b), N_2 (c), and He (d) in Cu-BTC at 298 K and 101 kPa, along with a schematic diagram of the two adsorption sites in Cu-BTC (e).
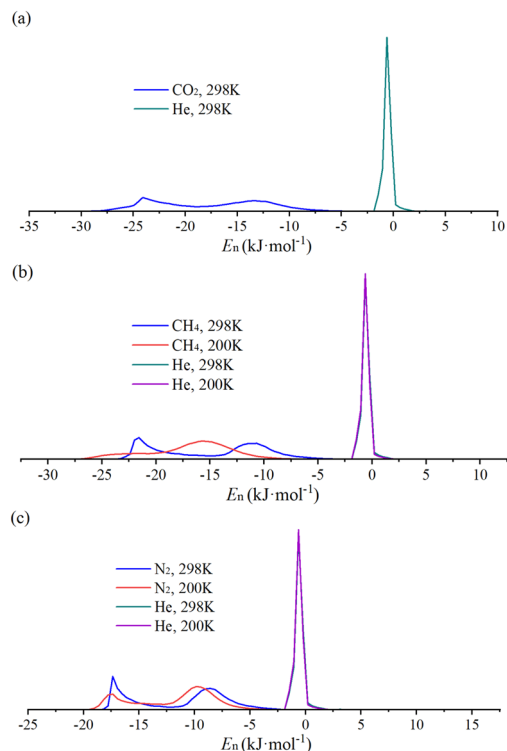
Fig. 6 Results of the adsorption energy distributions of CO_2 and He at 298 K and 101 kPa (a); CH_4 (b), N_2 (c), and He in Cu-BTC at 298 K and 200 K, 101 kPa.

Meanwhile, as shown in Fig. 6, due to the weak adsorption of He on Cu-BTC, there is an extremely small probability that its adsorption energy may even be greater than zero. In the adsorption energy distributions of CO_2, CH_4, and N_2 in Fig. 6, two peaks are observed, corresponding to the two adsorption sites A and B in Fig. 5(e). Since the adsorption affinity for He between the two sites is not significantly different, only one peak appears in the adsorption energy distribution for He in Fig. 6. According to Fig. 6(b) and (c), when the temperature is lowered to 200 K, the peaks for CH_4 and N_2 shift to the left. This is due to the decreased molecular kinetic energy at lower temperatures, leading to an enhanced confinement effect of the Cu-BTC framework on these adsorbates. For He, the peak shift is not significant, indicating that the confinement effect of the Cu-BTC framework on He does not increase markedly. This explains the significant increase in CH_4/He and N_2/He selectivity when the temperature is lowered.

DFT binding energy

The DFT binding energy is the binding energy between a single gas adsorbate molecule and an adsorption site within the adsorbent, calculated using density functional theory (DFT) at 0 K. It facilitates the assessment of variations in adsorption strength among different adsorption sites within the adsorbent for the same adsorbate molecule, as well as the differences in adsorption strength of the same adsorption site for different adsorbates. This helps in understanding the mechanism of

competitive adsorption. In this work, we conducted DFT calculations to determine the adsorption binding energies between two adsorption sites, A and B, in Cu-BTC (as shown in Fig. 5(e)), and the molecules CO_2, CH_4, N_2, and He. The binding energy reflects the strength of interaction between the adsorbate molecules and the adsorption sites. The adsorptive binding energy value is negative, and the larger its absolute value, the stronger the interaction between the adsorbent site and the adsorbate molecules. Geometric optimization was used to obtain the lowest energy adsorption configurations for each site and the four adsorbates. The configurations for site A are shown in Fig. 7(a)–(d), and those for site B are shown in Fig. S5(a)–(d).† The adsorption binding energies between each adsorbate molecule and sites A and B are listed in Table 2. According to the data in Table 2, for each adsorbate, the absolute value of the binding energy with site A is smaller than that with site B, indicating that site A has a weaker adsorption effect for the four adsorbates compared to site B. The binding energy difference between He and sites A and B is the smallest, consistent with previous calculations of adsorbate density distribution. Additionally, for each adsorption site, the order of binding energy magnitudes for the four adsorbates follows the trend $CO_2 > CH_4 > N_2 >$ He. This indicates that the affinity of adsorption sites in Cu-BTC for the four adsorbates follows the order $CO_2 > CH_4 > N_2 >$ He, which is consistent with previous research results. This also explains the mechanism of competitive adsorption in Cu-BTC for CO_2/He, CH_4/He, and N_2/He gas mixtures.

Adsorption breakthrough curves for CO_2/He, CH_4/He, N_2/He, and CH_4/N_2/He gas mixtures

The adsorption breakthrough curves for CO_2/He (50:50), CH_4/He (50:50), and N_2/He (50:50) gas mixtures in Cu-BTC
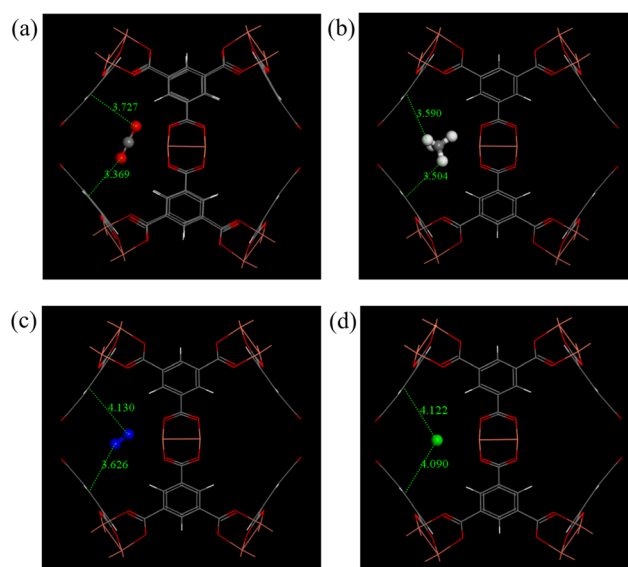

Fig. 7 The adsorption configurations of CO_2 (a), CH_4 (b), N_2 (c), and He (d) at site A in Cu-BTC. Atomic colors: C (gray), O (red), N (blue), H (white), Cu (orange), He (green).

Table 2 The binding energies between CO_2, CH_4, N_2, and He molecules and the A and B sites in Cu-BTC

Adsorbate	Adsorption site	Binding energy (kJ mol^{-1})
CO_2	A	−3.52
	B	−7.54
CH_4	A	−3.06
	B	−7.20
N_2	A	−2.54
	B	−6.46
He	A	−0.80
	B	−1.66

Table 3 The productivity of He from various helium-based gas mixtures at different temperatures, with the concentration of He in the product being greater than 99.999%

Helium-based gas mixture	Temperature (K)	He productivity (mol kg^{-1})
CO_2/He	298	0.6114
CH_4/He	298	0.0061
	200	1.9906
	150	9.6966
N_2/He	298	0.0002
	200	0.2840
	150	3.9692
CH_4/N_2/He	298	0.0004
	200	0.1881
	150	2.0970

are shown in Fig. 8(a)–(g). Because CO_2 has a relatively high boiling point and, according to previous research, Cu-BTC has already exhibited favorable selectivity for CO_2/He mixtures at 298 K, we therefore only measured the adsorption breakthrough curve of the CO_2/He mixture on Cu-BTC at 298 K. When the breakthrough times of the two components in the mixture differ significantly, *i.e.*, when the two breakthrough curves are far apart, the adsorbent exhibits better adsorption selectivity. According to Fig. 6, the breakthrough curve tests confirm that at the same

temperature, the adsorption selectivity of Cu-BTC follows the order CO_2/He > CH_4/He > N_2/He. Additionally, lowering the temperature can significantly enhance the adsorption and separation efficiency of Cu-BTC for various helium-based gas mixtures. In Fig. 6, there are instances where the ratio of the outlet to inlet concentration of some components exceeds 1. This phenomenon occurs due to competitive adsorption. As components with stronger adsorption affinity are continuously adsorbed, previously adsorbed components with weaker affinity are partially released due to the competition for adsorption sites, leading to an increase in their outlet concentration. In this study, we also performed integration of the adsorption breakthrough curves to calculate the productivity of He in various helium-based gas mixtures. This analysis aimed to evaluate the actual helium extraction performance of Cu-BTC for different gas mixtures. The calculation results are presented in Table 3. As shown in Table 3, lowering the temperature significantly improves the productivity of He in CH_4/He and N_2/He gas mixtures.

In this study, the adsorption breakthrough curves of the CH_4/N_2/He (33:33:33) ternary gas mixture in Cu-BTC were tested at 298 K, 200 K, and 150 K. The results are shown in Fig. S6(a)–(c).† Additionally, the productivity of He in the CH_4/N_2/He ternary gas mixture at different temperatures was calculated, as shown in Table 3. According to the data from Fig. S6† and Table 3, lowering the temperature significantly improves the adsorption separation efficiency of Cu-BTC for the CH_4/N_2/He ternary gas mixture and the He productivity.

Conclusions

In this study, to meet the demand for helium recovery from natural gas, a combined approach of molecular simulation and experimental methods were applied to investigate the adsorptive separation performance of the MOF material Cu-BTC for CO_2/He, CH_4/He, N_2/He, and CH_4/N_2/He gas mixtures at room and lower temperature. The main conclusions are as follows:

(1) From the simulation calculations and experimental tests of the single-component adsorption isotherms, it was found that the adsorption capacities of Cu-BTC for CO_2, CH_4,
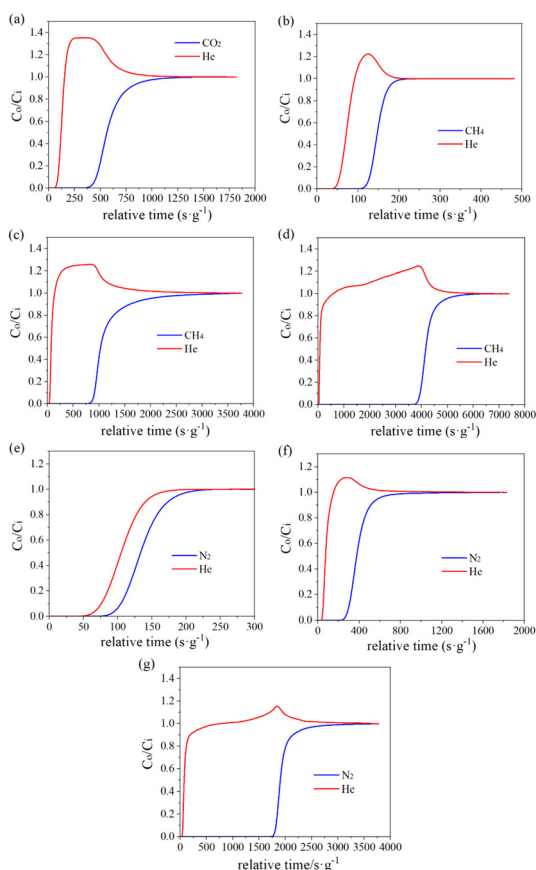

Fig. 8 The adsorption breakthrough curves of CO_2/He (50:50) at 298 K (a), CH_4/He (50:50) at 298 K (b), 200 K (c), and 150 K (d), and N_2/He (50:50) at 298 K (e), 200 K (f), and 150 K (g) in Cu-BTC tested at a pressure of 101.324 kPa. The *x*-axis represents the ratio of time to sample mass, and the *y*-axis represents the ratio of the outlet to inlet concentration of the components.

N_2, and He at the same temperature and pressure follow the order $CO_2 > CH_4 > N_2 > He$.

(2) Using IAST and GCMC simulations, the selective adsorption coefficients of Cu-BTC for CO_2/He, CH_4/He, and N_2/He were calculated, revealing that the selectivity follows the order $CO_2/He > CH_4/He > N_2/He$ at the same temperature and pressure. Additionally, lowering the temperature significantly enhances the selectivity and adsorption capacity of Cu-BTC for CH_4/He and N_2/He gas mixtures.

(3) To test the actual adsorptive separation performance of Cu-BTC, the adsorption breakthrough curves for CO_2/He, CH_4/He, N_2/He, and $CH_4/N_2/He$ gas mixtures in Cu-BTC were tested, further confirming that the selectivity of Cu-BTC at the same temperature and pressure follows the order $CO_2/He > CH_4/He > N_2/He$. Moreover, it was found that lowering the temperature significantly improves the separation efficiency and He productivity for CH_4/He, N_2/He, and $CH_4/N_2/He$ gas mixtures in Cu-BTC. At 150 K, the He productivities for CH_4/He $(50:50)$, N_2/He $(50:50)$, and $CH_4/N_2/He$ $(33:33:33)$ gas mixtures reached 9.9016 mol kg^{-1}, 4.0278 mol kg^{-1}, and 2.1284 mol kg^{-1}, respectively.

(4) To analyze the mechanism of competitive adsorption, molecular simulation methods were used to calculate the isosteric heat of adsorption, adsorption energy distribution, adsorbate density distribution, and adsorption binding energy of adsorbates at different adsorption sites. The difference in binding energy of different adsorbates at the same adsorption sites is the fundamental reason for competitive adsorption. In Cu-BTC, the open metal sites dominate its adsorption capacity for CO_2, CH_4, and N_2, as well as its adsorption selectivity toward helium-containing gas mixtures.

Data availability

This study was carried out using publicly available data from CCDC at https://www.ccdc.cam.ac.uk/structures/Search?Compound=HKUST-1&DatabaseToSearch=Published with 755080.

Author contributions

Shoucheng Cui: writing – original draft, validation, methodology, investigation, formal analysis, data curation, conceptualization. Baosheng Chen: writing – review & editing, visualization, data curation, supervision. Jiasi Zhao: writing – review & editing, data curation, supervision. Hongbo Xu: methodology, investigation, funding acquisition. Nan Peng: supervision, funding acquisition. Liqiang Liu: supervision, project administration.

Conflicts of interest

There are no conflicts to declare.

Acknowledgements

Notes and references

1 A. Karimi and M. A. Abdi, Selective Dehydration of High-Pressure Natural Gas Using Supersonic Nozzles, *Chem. Eng. Process.*, 2009, **48**, 560–568.

2 C. J. Berganza and J. H. Zhang, The Role of Helium Gas in Medicine, *Med. Gas Res.*, 2013, **3**, 18.

3 P. Zheng, W. Xie, Z. Cai, Y. Jiao, Y. Sun, T. Han, X. Ma, N. Li and S. Luo, Ionization of Tröger's Base Polymer of Intrinsic Microporosity for High-Performance Membrane-Mediated Helium Recovery, *J. Membr. Sci.*, 2023, **672**, 121425.

4 S. Tao, Y. Yang, Y. Chen, X. Liu, W. Yang, J. Li, Y. Wu, X. Tao, J. Gao, Y. Chen, X. Wang, X. Wu, X. Chen, Q. Li and J. Jia, Geological Conditions, Genetic Mechanisms and Accumulation Patterns of Helium Resources, *Pet. Explor. Dev.*, 2024, **51**(2), 498–518.

5 X. Wu, P. Jia, W. Jia and C. Li, A New Process for High-Efficiency Crude Helium Extraction and Purification from Natural Gas, *J. Nat. Gas Sci. Eng.*, 2024, **124**, 205278.

6 M. B. Kravchenko and G. K. Lavrenchenko, Non-Cryogenic Technology of Production of Helium Concentrate from Natural Gas, *Chem. Pet. Eng.*, 2020, **55**(11–12), 986–995.

7 A. F. Sahayaraj, H. J. Prabu, J. Maniraj, M. Kannan, M. Bharathi, P. Diwahar and J. Salamon, Metal-Organic Frameworks (MOFs): the Next Generation of Materials for Catalysis, Gas Storage, and Separation, *J. Inorg. Organomet. Polym.*, 2023, **33**, 1757–1781.

8 Y. Ma, H. Wang, H. Wang, J. Wang, S. Jiang, Q. Zheng, S. Jia, X. Li and T. Ma, A Stable Ultra-Microporous Hafnium-Based Metal-Organic Framework with High Performance for CO_2 Adsorption and Separation, *CrystEngComm*, 2023, **25**, 6489–6495.

9 A. L. Sutton, M. M. Sadiq, J. I. Mardel and M. R. Hill, Hydrogen Storage of Commercially Scalable CALF-20: A Study at Cryogenic and Near-Ambient Temperatures, *CrystEngComm*, 2024, **26**, 6003–6007.

10 S. Geng, C. Fu, X. Wang, Y. Yang, S. Wang, P. Ren and Z. Zhang, A Microporous Mn(II) MOF Based on 5-(4H-1,2,4-triazol-4-yl) Isophthalic Acid for CO_2/N_2 Separation, *Inorg. Chem.*, 2024, **63**, 8636–8641.

11 S. Gang, Z. Liu, S. Wu, S. Yang, R. Wang and J. Du, A Stable Zr(IV)-MOF for Efficient Removal of Trace SO_2 from Flue Gas in Dry and Humid Conditions, *J. Hazard. Mater.*, 2024, **470**, 134180.

12 H. Tang, Q. Xu, M. Wang and J. Jiang, Rapid Screening of Metal-Organic Frameworks for Propane/Propylene Separation by Synergizing Molecular Simulation and Machine Learning, *ACS Appl. Mater. Interfaces*, 2021, **13**, 53454–53467.

13 W. Xie, L. Yang, J. Zhang and X. Zhao, The Adsorptive Separation of Ethylene from C2 Hydrocarbons by Metal-Organic Frameworks, *Chem. – Eur. J.*, 2023, **29**, e202300158.

14 Y. Li, Y. Situ, K. Guan, Y. Guan, X. Huang, C. Cai, S. Li, Z. Liu, H. Liang, Y. Wu, Q. Yang and Z. Qiao, High Dynamic Separation Performance of Metal-Organic Frameworks for D_2/H_2: Independent or competitive adsorption?, *AIChE J.*, 2024, **70**, e18283.

15 O. Kadioglu and S. Keskin, Efficient Separation of Helium from Methane Using MOF Membranes, *Sep. Purif. Technol.*, 2018, **191**, 192–199.

16 J. Wang, Y. Li, Y. Yang, Y. Li, M. Zhao, W. Li, J. Guan and Y. Qu, Efficient Helium Separation with Two-Dimensional Metal-Organic Framework Fe/Ni-PTC: A Theoretical Study, *Membranes*, 2021, **11**, 927.

17 I. V. Grenev and V. Y. Gavrilov, High-Throughput Screening of Metal-Organic Frameworks for Helium Recovery from Natural Gas, *Microporous Mesoporous Mater.*, 2024, **368**, 113021.

18 C. Fu, Y. Guo, J. Luo, Z. Qi, T. Qi and G. Hu, Separation of Methane, Nitrogen, and Helium Using a Layered Triple-Reflux Pressure Swing Adsorption, *Ind. Eng. Chem. Res.*, 2025, **64**, 639–649.

19 R. Vysyaraju, J. A. Sawada, L. E. Perez and A. Rajendran, Simulation and Experimental Demonstration of Helium Purification from He/N_2 Mixtures by Pressure Swing Adsorption, *Chem. Eng. J.*, 2024, **499**, 155929.

20 R. Weh, G. Xiao, E. S. Pouya and E. F. May, Direct Helium Recovery from Natural Gas by Dual Reflux Pressure Swing Adsorption Cascade, *Chem. Eng. J.*, 2022, **450**, 137894.

21 S. Shang, Z. Tao, C. Yang, A. Hanif, L. Li, D. C. W. Tsang, Q. Gu and J. Shang, Facile Synthesis of CuBTC and Its Graphene Oxide Composites as Efficient Adsorbents for CO_2 Capture, *Chem. Eng. J.*, 2020, **393**, 124666.

22 L. Ansone-Bertina, V. Ozols, L. Arbidans, L. Dobkevica, K. Sarsuns, E. Vanags and M. Klavins, Metal-Organic Frameworks (MOFs) Containing Adsorbents for Carbon Capture, *Energies*, 2022, **15**, 3473.

23 T. Qiu, S. Gao, Y. Fu, D. Xu and D. Kong, Template-Mediated Synthesis of Hierarchically Porous Metal-Organic Frameworks for Efficient CO_2/N_2 Separation, *Materials*, 2022, **15**, 5292.

24 F. A. Kloutse, W. Gauthier, A. Hourri, S. Natarajan, P. Benard and R. Chahine, Study of Competitive Adsorption of the N_2O-CO_2-CH_4-N_2 Quaternary Mixture on CuBTC, *Sep. Purif. Technol.*, 2020, **235**, 116211.

25 A. Akbari, J. Karimi-Sabet and S. M. Ghoreishi, Intensification of Helium Separation from CH_4 and N_2 by Size-Reduced Cu-BTC Particles in Matrimid Matrix, *Sep. Purif. Technol.*, 2020, **251**, 117317.

26 D. Nazarian, J. S. Camp and D. S. Sholl, A Comprehensive Set of High-Quality Point Charges for Simulations of Metal-Organic Frameworks, *Chem. Mater.*, 2016, **28**, 785–793.

27 S. Fakhraie, H. R. Rajabi and A. Rashidi, Fabrication and Application of Novel Core-Shell MIL-101(Cr)@UiO-66(Zr) Nanocrystals for Highly Selective Separation of H_2S and CO_2, *Chem. Eng. J.*, 2023, **452**, 139001.

28 X. Du, D. Pang, Y. Cheng, Y. Zhao, Z. Hou, Z. Liu, T. Wu and C. Shu, Adsorption of CH_4, N_2, CO_2, and Their Mixture on Montmorillonite with Implications for Enhanced Hydrocarbon Extraction by Gas Injection, *Appl. Clay Sci.*, 2021, **210**, 106160.

29 S. Borocci, F. Grandinetti and N. Sanna, From LAr to L-ArBeO (L = He, Ne, Ar, HF): Switching on σ-hole Effects in Non-Covalent Interactions, *Chem. Phys. Lett.*, 2021, **768**, 138402.

30 C. Gong, X. Peng, M. Zhu, T. Zhou, L. You, S. Ren, X. Wang and X. Gu, Synthesis and Performance of STT Zeolite Membranes for He/N_2 and He/CH_4 Separation, *Sep. Purif. Technol.*, 2022, **301**, 121927.

31 Y. Zhang, T. L. Saleman, G. K. Li, G. Xiao, B. R. Young and E. F. May, Non-isothermal Numerical Simulations of Dual Reflux Pressure Swing Adsorption Cycles for Separating N_2 + CH_4, *Chem. Eng. J.*, 2016, **292**, 366–381.

32 H. Yang, C. Yin, B. Jiang and D. Zhang, Optimization and Analysis of A VPSA Process for N_2/CH_4 Separation, *Sep. Purif. Technol.*, 2014, **134**, 232–240.

33 P. M. Mathias, R. Kumar, J. D. Moyer, J. M. Schork, S. R. Srinivasan, S. R. Auvil and O. Talu, Correlation of Multicomponent Gas Adsorption by the Dual-site Langmuir Model Application to Nitrogen/Oxygen Adsorption on 5A-Zeolite, *Ind. Eng. Chem. Res.*, 1996, **35**, 2477–2483.

34 C. Xin, S. Hou, L. Yu, X. Zhou, Y. Fu, X. Yang, W. Sun, F. Yang, X. Wang and L. Liu, Controlled Synthesis of Mg-MOF-74 and Its CO_2 Adsorption in Flue Gas, *Coatings*, 2024, **14**, 383.

35 J. Sim, H. Yim, N. Ko, S. B. Choi, S. Oh, H. J. Park, S. Park and J. Kim, Gas Adsorption Properties of Highly Porous Metal-Organic Frameworks Containing Functionalized Naphthalene Dicarboxylate Linkers, *Dalton Trans.*, 2014, **43**, 18017.

36 S. Ullah, M. A. Bustam, M. A. Assiri, A. G. Al-Sehemi, M. Sagir, F. A. A. Kareem, A. E. I. Elkhalifah, A. Mukhtar and G. Gonfa, Synthesis, and Characterization of Metal-Organic Frameworks-177 for Static and Dynamic Adsorption Behavior of CO_2 and CH_4, *Microporous Mesoporous Mater.*, 2019, **288**, 109569.

37 N. Singh, S. Dalakoti, A. Sharma, R. Chauhan, R. S. Murali, S. Divekar and S. Dasgupta, Aarti, Shaping of MIL-53-Al and MIL-101 MOF for CO_2/CH_4, CO_2/N_2 and CH_4/N_2 Separation, *Sep. Purif. Technol.*, 2024, **341**, 126820.

38 J. S. Lee, S. H. Jhung, J. W. Yoon, Y. K. Hwang and J.-S. Chang, Adsorption of Methane on Porous Metal Carboxylates, *J. Ind. Eng. Chem.*, 2009, **15**, 674–676.

39 Z. Tao, Y. Tian, A. Hanif, V. Chan, Q. Gu and J. Shang, Metal cation-exchanged LTA Zeolites for CO_2/N_2 and CO_2/CH_4 Separation: The Roles of Gas-Framework and Gas-Cation Interactions, *Carbon Capture Sci. Technol.*, 2023, **8**, 100126.

40 J. Koubek, J. Pašek and J. Volf, The Isosteric Heat of Adsorption on Heterogeneous Surfaces, *J. Colloid Interface Sci.*, 1975, **51**(3), 491–498.

41 S. A. Al-Muhtaseb and J. A. Ritter, Roles of Surface Heterogeneity and Lateral Interactions on the Isosteric Heat of Adsorption and Adsorbed Phase Heat Capacity, *J. Phys. Chem. B*, 1999, **103**, 2467–2479.